ChemCatChem

Research Article
doi.org/10.1002/cctc.202501178

Chemistry Europe
European Chemical Societies Publishing

www.chemcatchem.org

Unveiling the Role of Manganese Substitution in Nanocast Cobalt Oxide for Alkaline Water Electrolysis Performance

Jean Pascal Fandré,[a] Eko Budiyanto,[a] Ashwani Kumar,[a] and Harun Tüysüz*[a, b]

The design and development of next-generation electrocatalysts, coupled with an in-depth understanding of their structural dynamics under operating conditions, are critical for advancing the efficiency and durability of water electrolysis technologies for green hydrogen production. Herein, the impact of manganese substitution on the morphology, electronic structure, and oxygen evolution reaction (OER) activity of cobalt-based spinel oxides is investigated. Two-dimensional mesoporous cobalt manganese oxides synthesized by the hard-templating method using SBA-15 silica templates are utilized as a well-defined model material system. At the highest Mn content, the aligned mesoporous structure is found to be significantly less ordered. X-ray absorption and Raman spectroscopies indicate that Mn mainly occupies the octahedral sites. OER survey shows that even small amounts of Mn substitution of Co can significantly decrease the OER performance of the catalysts due to the prevention of active species formation. Electrochemical impedance, in situ Raman spectroscopy, ICP-OES, and post-mortem XRD indicate that above 1.4 V versus RHE, Mn leaches from the bulk spinel octahedral site.

1. Introduction

In order to limit global warming to 2 °C and achieve net-zero carbon emissions by 2050, important industrial sectors must be decarbonized.[1] Green hydrogen, produced through water electrolysis using renewable energy, can significantly contribute to the decarbonization of industrial sectors that are challenging to electrify or decarbonize by other means. Promising sectors that can be decarbonized with green hydrogen include plastic, fertilizer, and steel production.[2] Water splitting is an endothermic reaction consisting of two half-reactions, the hydrogen evolution reaction (HER) and the oxygen evolution reaction (OER), which occur at the cathode and anode, respectively. The OER is the major bottleneck due to its slow kinetics and the considerable overpotential required. This overpotential often leads to the oxidation of the catalyst, which is why metal oxides are considered the most potent catalysts in terms of long-term stability.[3] Large-scale preparation for industrial catalyst use is more feasible for transition metal oxides (TMOs) than for other oxides, making TMOs the most appealing for practical utilization.[3] However, the last significant breakthrough in this field at the level of industrial commercialization occurred in 1987 when D. A. Corrigan accidentally formed a highly active Ni—Fe oxide electrocatalyst.[4] Although cobalt oxide catalysts are effective OER catalysts,[3] they are expensive[5,6] and have low conductivity.[7] Therefore, substituting cobalt with cheaper and more conductive elements has been the focus of recent studies.

Among different transition metals, manganese appears to be a good candidate since it is an earth-abundant and inexpensive metal. It has also been demonstrated to enhance the electrical conductivity of Mn-substituted Co oxides.[8] Recently, it was shown that Mn enhances the stability of spinel Co oxides in both acidic[9] and alkaline[10] electrolytes through the partial substitution of Co with Mn. However, the precise role of Mn within Co oxide structures remains ambiguous and is still a matter of debate.[11,12] This has led to conflicting claims in the literature regarding the influence of Mn incorporation on the activity of Co oxides for OER. Chartier et al. claims that Mn negatively impacts OER performance,[13] while Risch et al. claims that Mn has a negligible impact on performance but enhances the long-term stability.[10] At the other end of the spectrum, Molin et al.[14] and Li et al.[15] demonstrate that Mn positively impacts OER performance. These conflicting claims make it impossible to predict the influence of adding Mn on activity, stability, and other properties in advance. A well-defined model system spanning a broad compositional range is crucial for the rigorous evaluation of electrocatalysts for OER.

Most of the synthetic methodologies for varying the composition of the materials result in also a variation in other physical and chemical properties, which makes it challenging to relate the change of the catalytic performance to the compositional alteration. For instance, Chartier et al. prepared cobalt–manganese oxide powders via thermal decomposition, which has no control on the morphology, domain, and crystal-

[a] J. P. Fandré, E. Budiyanto, A. Kumar, H. Tüysüz
Department of Heterogeneous Catalysis, Max-Planck-Institut für Kohlenforschung, Kaiser-Wilhelm-Platz 1, Mülheim an der Ruhr 45470, Germany
E-mail: tueysuez@kofo.mpg.de
harun.tuysuz@imdea.org

[b] H. Tüysüz
Catalysis and Energy Materials Group, IMDEA Materials Institute, Tecnogetafe, Calle Eric Kandel, 2, Getafe, Madrid 28906, Spain

Supporting information for this article is available on the WWW under https://doi.org/10.1002/cctc.202501178

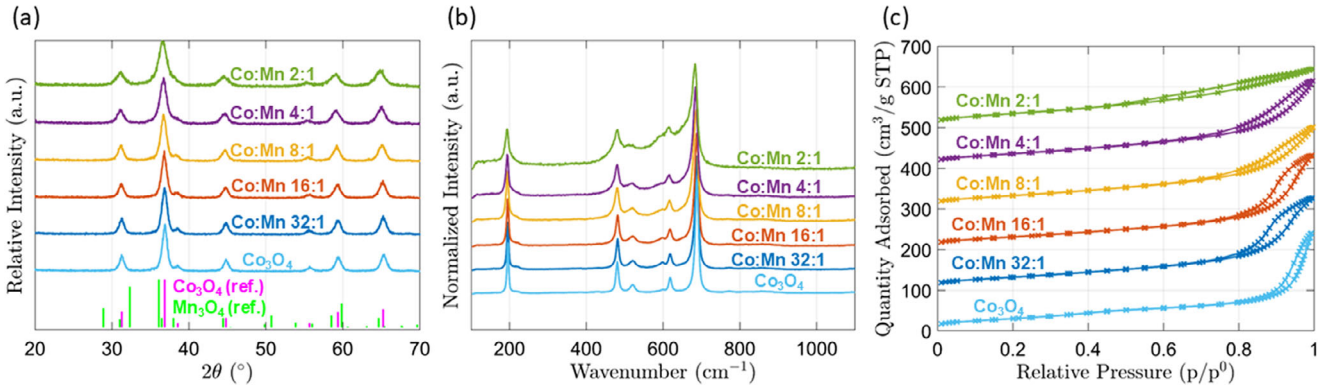

Figure 1. a) Wide-angle XRD pattern of pristine Co_3O_4 and different Co:Mn ratio oxides. The Co_3O_4 reference (ICSD Entry: 24210[21]) is given in purple and the Mn_3O_4 reference (ICSD Entry 68174[22]) is given in bright green. b) Raman spectra of pristine Co_3O_4 and different Co:Mn ratio oxides. c) N_2 physisorption isotherms of the sample series, offset is 100 cm^3/g.

lite size.[13] Risch et al. prepared cobalt–manganese oxide films via electrodeposition, with very limited control on surface morphology, particle size, and crystallinity.[10] Molin et al. synthesized cobalt–manganese oxide powders via a sol–gel method [14] and Li et al. synthesized particles using a hot-injection method,[15] both of the methods result in deviation of morphology and structural properties with the variation of the composition. On the other hand, the nanocasting (hard templating) method can be used as an excellent model system to control the morphology, particle size, and textural parameters when Mn is substituted in large amounts. Additionally, the absence of surfactants during synthesis enables the production of clean surfaces for targeted replicas. The nanocasting method typically involves three main steps: synthesis of the template, impregnation and calcination, and selective removal of the template.[16,17] In contrast to previous studies, the use of this model system can enable a clear elucidation of the distinct compositional roles of cobalt and manganese oxides in OER.

Herein, we systematically explore the impact of Mn incorporation on the morphology, electronic structure, and OER activity of Mn-substituted cobalt oxide spinels across a broad compositional range, highlighting previously unreported compositional effects in a well-defined model system. The well-defined sample series is prepared via the nanocasting route by using SBA-15 silica as a template. Using a mesoporous hard template ensures a periodic pore structure, rigid morphology, and similar textural parameters independent of the composition. These properties are all crucial for obtaining reliable data and gaining fundamental insight into the material system.

2. Results and Discussion

Two-dimensional ordered mesoporous cobalt–manganese oxides with various compositions were synthesized via the nanocasting method using SBA-15 as the hard template. The samples are denoted by their Co:Mn ratios, e.g. Co:Mn 16:1, meaning the sample contains 16 parts cobalt and 1 part manganese. Wide-angle XRD patterns displayed well-resolved reflections of a phase-pure, crystalline, cubic cobalt oxide spinel phase (Figure 1a). As the Mn content increases, the reflections shift to lower angles due to a change in lattice parameter, indicating the successful incorporation of Mn into the lattice (Figure S1). Raman spectroscopy measurements complement the XRD results, showing the five typical bands of cubic cobalt oxide spinel (Figure 1b). The five bands are as follows: the F_{2g} bands (~195, 520, and 620 cm^{-1}), the E_g band (~480 cm^{-1}) and the A_{1g} band (~690 cm^{-1}).[18] Of these five bands, only the A_{1g} has a direct correlation to a single site in the lattice, namely the octahedral site.[19] The other four bands are a mix of the phonons of both the tetrahedral and the octahedral sites. As the Mn content increases, the A_{1g} band shifts to lower wave numbers, due to the lower vibrational frequency by incorporation of a larger size Mn ion compared to a Co ion of the same charge. This indicates a successful integration of Mn into the octahedral site of the spinel. Additionally, there is a band visible at ~600 cm^{-1}, which might be from a hydroxide phase due to the immersion in 2 M NaOH during SBA-15 silica leaching. To confirm this, a second Co:Mn 2:1 sample was synthesized via a carbon template, eliminating the necessity of a leaching step with an alkaline solution during synthesis (Figure S2). There is a clear difference visible in the region around 600 cm^{-1} denoting the influence of the alkaline leaching step on the formation of metal hydroxide on the surface.

Nitrogen physisorption measurements were performed to analyze the mesoporous structure of the nanocast samples. A type IV(a) isotherm, as defined by the IUPAC classification,[20] was observed for all samples (Figure 1c), which indicates a mesoporous structure. A significant difference between the samples is observed at a relative pressure of 0.5–1.0 p/p°, where, with increasing Mn content, the pore volume decreases and the pore size distribution broadens (Figure S3a). This is consistent with the decrease in ordering degree of the mesoporous samples observed with increasing Mn content (Figure 2). The BET surface area of the nanocast pristine Co_3O_4 was 114 m^2/g, increasing slightly with increasing Mn content to reach a maximum of 134 m^2/g for the Co:Mn 2:1 sample (Table S1). As previously mentioned, the pore volume decreased from 0.37 cm^3/g for the pristine Co_3O_4 to 0.23 cm^3/g for the Co:Mn 2:1 sample (Table S1).

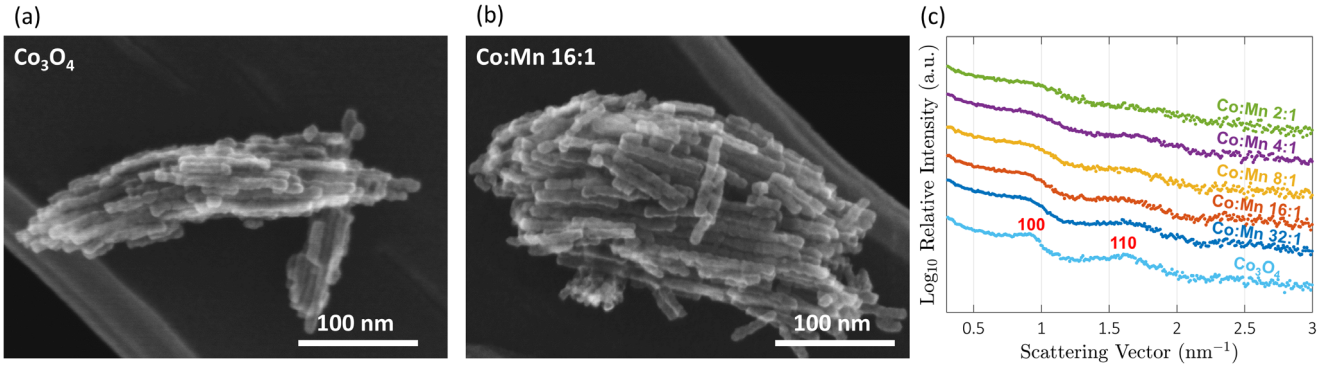

Figure 2. a) SEM micrograph showing ordered mesoporous Co_3O_4. b) SEM micrograph showing Co:Mn 16:1 and its mesostructure. c) SAXS data for pristine Co_3O_4 and different Co:Mn ratio oxides.

An electron microscopy survey was performed to visualize morphology and confirm the successful negative replication of the SBA-15 template (Figure 2a,b). For the pristine Co_3O_4, large, well-ordered mesostructured domains could be observed (Figure S4a). In comparison, smaller, less ordered mesostructured domains were observed in the Mn-containing samples. Additionally, the length of the nanowires decreased with increasing Mn content (see Figure S4b). For pristine Co_3O_4, the typical nanowire length observed was approximately 100 nm, while for Co:Mn this was approximately 30 nm. The measured nanowire diameter, ca. 9 nm, did not change with Mn content and matches well the measured pore size of the SBA-15 template (Figure S3b). The domain structure also became denser with increasing Mn content due to the lower degree of interconnectivity of the nanowires (Figure S4b). This denser domain structure explains the decrease in pore volume with increasing Mn content, as measured by N_2 physisorption. Furthermore, in addition to the mesopores created by the voids between the nanowires, larger mesopores were observed, originating from the random stacking of small domains on top of one another. This explains the secondary peak in the pore size distribution of Co_3O_4 and why this second peak shifts towards lower pore sizes and disappears at the highest Mn content. TEM imaging (Figure S11a–f) reveals that partial substitution of Co with Mn leads to a denser microstructure with disordered nanowires domains, which may influence active site distribution and catalytic behavior. High-resolution TEM (HRTEM) and the corresponding fast Fourier transform (FFT) analysis (Figure S12a–c) confirm that the as-synthesized materials retain high crystallinity despite the induced morphological disorder. Furthermore, bulk SEM–EDX measurements (Figure S13) and STEM–EDX elemental mapping (Figure S14) indicate that the measured Co:Mn atomic ratio is in close agreement with the nominal composition, with both elements distributed in close proximity throughout the catalyst particles at nanoscales.

Synchrotron-based X-ray absorption spectroscopy (XAS) was used to determine the oxidation state of the Mn cations. The *K*-edge spectra consist of two regions, the pre-edge region and the main edge. The pre-edge region is due to the 1s to 3d transitions and provides information about the geometric and electronic features. The main edge is due to the 1s to 4p transition. By comparing the main edges of the different cobalt–manganese oxides, the average oxidation state of each element can be determined (Figure 3). The relationship between edge–energy positions and formal oxidation state is nearly linear.[23] However, the correlation between edge energy and the formal oxidation state of an element is purely empirical.[23] Using a calibration curve (Figure S6), the average oxidation state of the Mn was determined to be around 3.7–4.0, where average oxidation state decreased with increasing Mn content, resulting in the highest Mn^{4+}/Mn^{3+} ratio for a Co:Mn 32:1 and the lowest ratio for a Co:Mn 2:1, with Co:Mn 8:1 probably an outlier. The mixed valence states of Mn in cobalt–manganese spinels have been extensively reported in the literature; however, the actual Mn^{4+}/Mn^{3+} ratio is highly dependent on the synthesis route and subsequent thermal treatment. Low-temperature approaches, such as electrodeposition, typically favor a higher Mn^{4+}/Mn^{3+} ratio, whereas high-temperature precursor decomposition methods promote the stabilization of Mn^{3+} species.[8,10,13] Employing a thermal treatment step analogous to that used in the present study yielded comparable results in terms of the average Mn oxidation state, as well as a consistent trend with increasing Mn content.[24]

Subsequent to structural characterization, their OER performances are further investigated in a 1 M KOH electrolyte. Firstly, linear sweep voltammetry (LSV) was used to screen the OER activity after conditioning the catalyst with 50 cyclic voltammetry (CV) cycles. The LSV curves of the different cobalt–manganese oxides are shown in Figure 4a. The overpotential necessary to reach 10 mA/cm^2 (Figure S5a), chosen based on the current drawn by a solar-to-fuel device with 10% efficiency under one-sun illumination,[25] and the current density at 1.7 V versus RHE were used as OER activity indicators. As seen in Figure 4a, with increasing Mn amount, the OER activity decreases significantly. While pristine Co_3O_4 reaches a current density of 150 mA/cm^2 at 1.7 V versus RHE, Co:Mn 16:1 reaches only 100 mA/cm^2, roughly 2/3 of the current density achieved by the pristine catalyst. Co:Mn 2:1 achieves the lowest current density at 1.7 V versus RHE and does not even reach 10 mA/cm^2. Mn^{3+} is thought to be the active state for the OER; however, small amounts of Mn^{4+} are beneficial for performance, while a predominance of Mn^{4+} negatively impacts the OER performance.[26] The predominance of Mn^{4+}, as determined by XAS, could explain the significant decrease in OER performance. The superior activity of the Co:Mn 32:1 sample compared to other

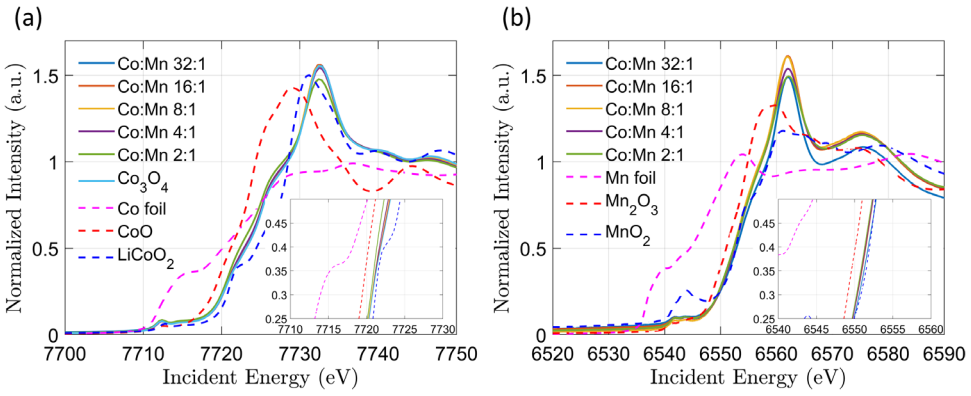

Figure 3. a) Normalized Co *K*-edge XANES spectra of pristine Co_3O_4 and different Co:Mn ratio oxides, as well as different reference materials (metallic Co(0) foil, Co(II)O and $LiCo(III)O_2$). The inset shows the edge of the measured materials near the half-edge step. b). Normalized Mn *K*-edge XANES spectra of different Co:Mn ratio oxides and different reference materials (metallic Mn(0) foil, $Mn(III)_2O_3$ and $Mn(IV)O_2$). The inset shows the edge of the measured materials near the half-edge step.

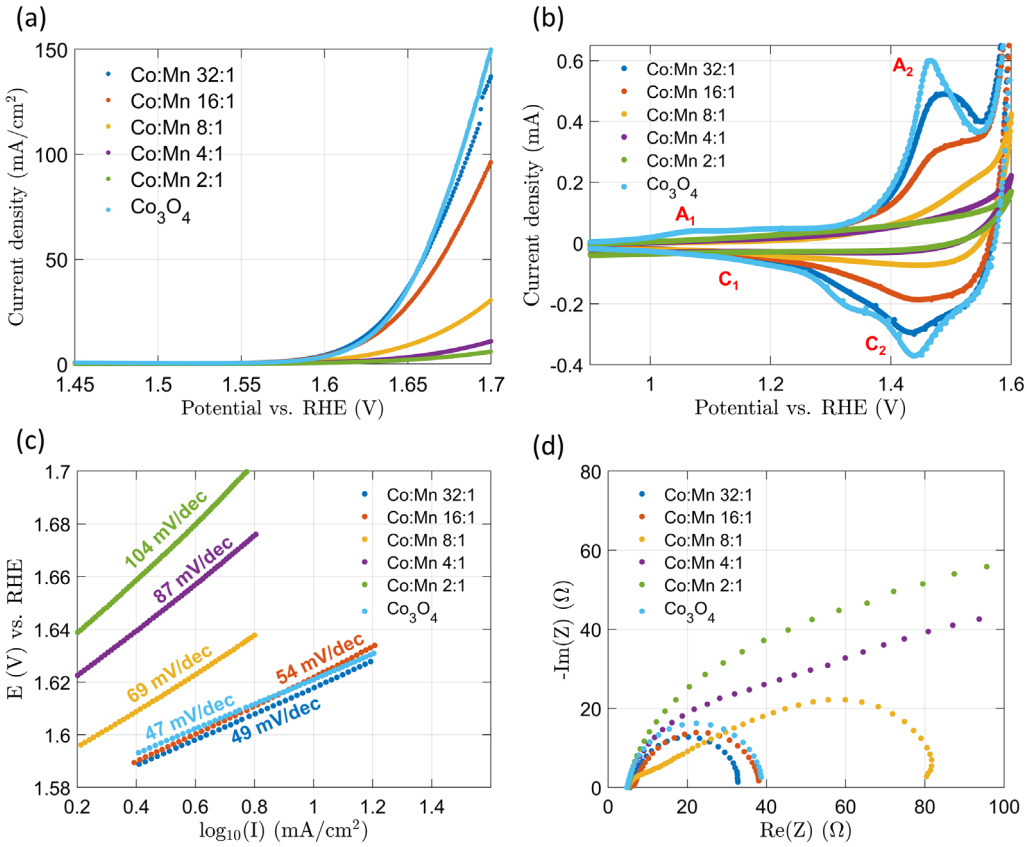

Figure 4. OER performance of nanocast cobalt–manganese oxides: a) LSV of pristine Co_3O_4 and different ratios Co:Mn oxides in 1 M KOH at 25 °C. b) CV at 50th cycle with a scan rate of 50 mV/s. c) Calculated Tafel slopes values of pristine Co_3O_4 and different ratios Co:Mn oxides. d) Nyquist plots.

Co:Mn compositions can be attributed to its low manganese content, despite exhibiting the highest average Mn oxidation state. Further, it is believed that irreversible activity loss in the case of Mn primarily stems from the oxidation of Mn.[27] Mn dissolution from the catalyst material is a common cause of low stability; however, the corrosion behavior of Mn strongly depends on the electrolyte.[28]

The Tafel slopes (calculated from the LSVs) show that as the Mn content increases, the Tafel slopes increase from the typical value of 47 mV/dec found for spinel cobalt oxide catalysts[29–32] to about 100 mV/dec. The Co:Mn 2:1 sample exhibited the highest Tafel slope, indicating the slowest kinetics among the tested cobalt-manganese oxides (Figure 4c). In addition to providing information on kinetics, Tafel slopes can also offer insights into the underlying mechanism. The notable difference between the Tafel slopes of Co_3O_4 and Co:Mn 2:1 suggests that either the rate-determining step (RDS) of the OER mechanism has changed or that the mechanism itself has shifted. To investigate a potential

change of the mechanism from the lattice oxygen mechanism (LOM) to the adsorbate evolution mechanism (AEM), two cobalt–manganese oxide samples were screened for their OER activity in 1 M tetramethylammonium hydroxide (TMAOH) and compared to pristine Co_3O_4 (Figure S5b). This was done as TMA^+ can be used as a chemical probe that is known for its specific interaction with negatively charged species and inhibiting the LOM cascade.[33–35] All three samples displayed reduced OER activity in the presence of TMAOH, indicating partial inhibition of the LOM pathway due to the strong electrostatic interaction between TMA+ and negative oxygenated intermediates.[33–35] This suggests that the pronounced difference in Tafel slopes between Co_3O_4 and Co:Mn 2:1, likely arises from a change in the RDS rather than a transition from the LOM to the AEM. Additionally, the strongly reduced OER activity of the cobalt-manganese oxides in TMAOH could hint at a reduced number of active sites when compared to the slight reduction of OER activity of pristine Co_3O_4.

Comparing the 50th cycle of CV it revealed that, with increasing Mn content, the A_2 anodic peak, typically observed at 1.46 V versus RHE for pristine Co_3O_4 indicating the oxidation of Co^{3+} to Co^{4+}, was suppressed and shifted to a higher potential (Figure 4b). The shift to a higher potential could be explained by the overall more stable Co—O bond in the mixed oxide.[9] All of this resulted in a CV of Co:Mn 2:1 exhibiting non-Faradaic-like behavior, largely due to the absence of significant chemical reactions at the surface. A suppressed A_2 anodic peak hints at a decrease in the oxidation of Co^{3+} to the active Co^{4+} species. This could explain the significantly worse performance of Co:Mn 2:1 compared to pristine Co_3O_4, even though only half of the Co^{3+} was replaced. Electrochemical impedance spectroscopy (EIS) was performed in the final step of the OER activity screening. For Co:Mn ratios of 32:1 and 16:1, the charge-transfer resistance is slightly lower compared to pristine Co_3O_4 (Figure 4d). This reduction can be rationalized within the framework of mixed-valence semiconductors, where electrical conductivity arises from hopping of charge carriers between Mn^{3+} and Mn^{4+} ions.[8] The charge-transfer resistance was determined by fitting the impedance data: Co_3O_4 and Co:Mn = 32:1 were well described by a simple Randles circuit, whereas Co:Mn = 8:1 and Co:Mn = 2:1 required a modified Randles circuit due to the presence of two semicircles in the Nyquist plots (Figure S15).[36–38] In this model, the high-frequency semicircle is typically associated with the resistance of an inner electrode layer, while the low-frequency semicircle corresponds to the resistance of an outer surface layer.[36–38] The extracted fitting parameters are summarized in Table S3. Notably, the emergence of a pronounced low-frequency semicircle with increasing Mn content suggests the formation of a less conductive secondary surface phase on the catalyst.

To investigate the catalyst surface in more detail, in situ Raman spectroscopy was performed under the same conditions as the OER activity screening (Figure 5). Pristine Co_3O_4 exhibits no changes detectable by Raman spectroscopy within the potential range of 1.0 V to 1.55 V versus RHE (Figure 5a,c). In this case, the formation of CoOOH under OER conditions could not be captured by in situ Raman spectroscopy, due to the bulk spinel dominating the gathered Raman spectra. In addition, the catalyst film deposition by drop casting is in the micrometer range, hindering the surface sensitivity, unlike the monolayer deposition methods as reported in Bell et al.[39] and Hu et al.[40] In contrast, Co:Mn 2:1 undergoes visible changes when a potential bias is applied (Figure 5b,d). Above 1.45 V versus RHE, a new band appears slightly below 600 cm^{-1} (Figures 5b and S7), while the A_{1g} band simultaneously shifts to higher wavenumbers (Figure 5d), unlike pristine Co_3O_4 (Figure 5c). The blue shift of the A_{1g} band partially reverses the shift previously observed with Mn incorporation into Co_3O_4 (Figure S8). Post-mortem XRD performed in Co:Mn 2:1 after 24 h at 1.6 V vs. RHE also shows a shift of the reflections to a higher angle (Figure S10). The shift of the A_{1g} bands is permanent and remains at the same wavenumber, even after 50 CV cycles and drying the sample again (Figure S9). Additionally, no significant Mn content was detected in the electrolyte, eliminating the possibility of large-scale Mn leaching (Table S2). Post-mortem XPS performed on the same samples as for XRD reveals a slightly lower Mn surface content, more Co^{3+}, likely from formed CoOOH, and no change in the Mn 2p peak that closely resembles MnOOH (Figure S11).

3. Conclusion

In this study, we systematically investigated the effect of manganese substitutions in cobalt oxide using nanocast cobalt manganese oxide nanowires as a well-defined model system. The incorporated Mn content played a decisive role in modifying the morphology, electronic structure, and OER performance of the material. Increasing Mn levels led to the formation of shorter nanowires and a larger domain structure, while at the highest Mn content, the mesoporous ordering was substantially disrupted. X-ray absorption and Raman spectroscopy analyses revealed that Mn predominantly occupies octahedral coordination sites, exhibiting an average oxidation state between +3.7 and +4.0. Electrochemical screening demonstrated that even minor Mn substitution negatively impacts the OER activity, suggesting a detrimental effect on the catalytic performance. Electrochemical impedance spectroscopy further indicated the formation of a less conductive second phase on the surface at higher Mn concentrations, as evidenced by the emergence of a second semicircle in the Nyquist plots. In situ Raman spectroscopy revealed Mn leaching from the bulk octahedral sites at potentials above 1.4 V versus RHE, along with the appearance of a new spectral band.

4. Experimental Section

4.1. Synthesis of SBA-15 Silica Template

The SBA-15 silica template was synthesized according to the reported protocol.[17] In the first step, 27.8 g of Pluronic P-123 (avg. $M_n \sim 5800$; Sigma-Aldrich) was dissolved in 504 mL of distilled water in a 1 L autoclavable PP bottle, then 15.5 g of HCl (37%–38%; J.T. Baker) was added to the solution, which was then stirred at 35 °C for one hour. Then, 60 g of tetraethyl

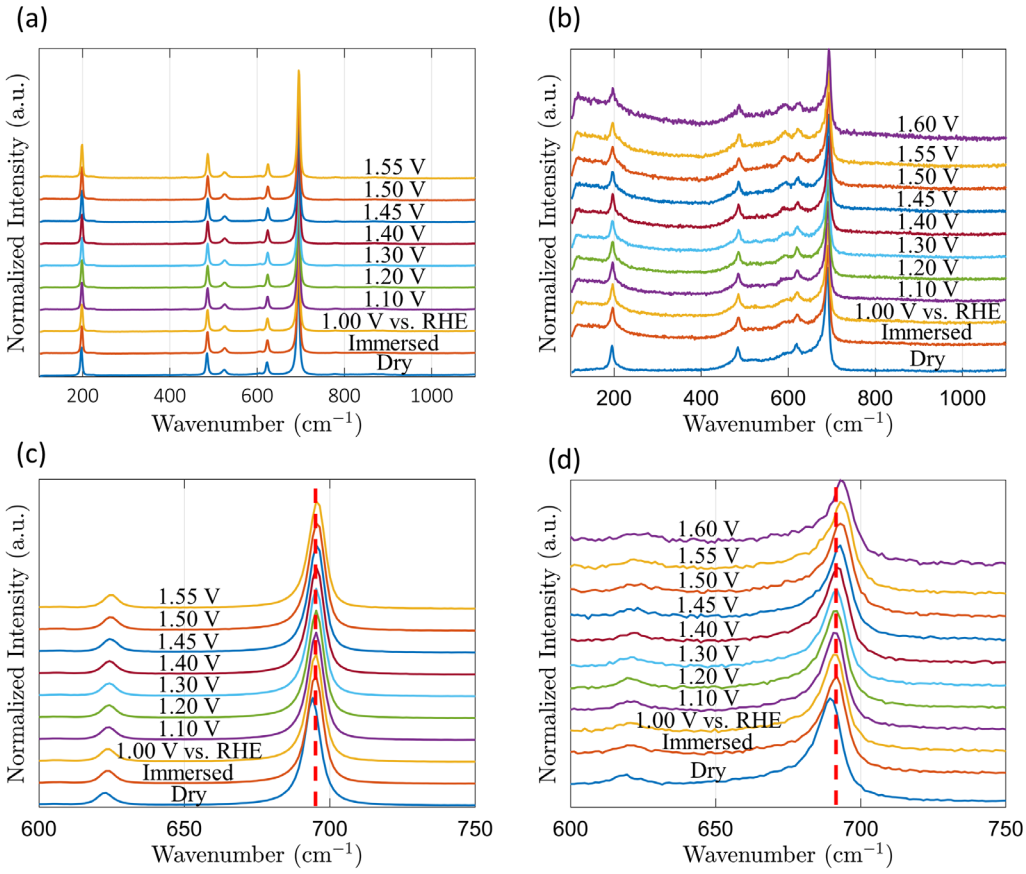

Figure 5. In situ Raman spectra of pristine Co_3O_4 and Co:Mn 2:1 recorded between 1.0-1.6 V versus RHE. a) Series of Raman spectra showing the evolution of Co_3O_4 under OER conditions. b) Series of Raman spectra showing the evolution of Co:Mn 2:1 under OER conditions. c) Enlarged part of a) to show the A_{1g} band in more detail. d) Enlarged part of b) to show A_{1g} band in more detail.

orthosilicate (TEOS, reagent grade, 98%; Sigma-Aldrich) was added, under stirring. The solution was stirred continuously for another 24 h at 35 °C, followed by a hydrothermal treatment at 100 °C for another 24 h. The precipitate was collected by vacuum filtration and dried at 100 °C overnight. Before calcination, the product was finely crushed and then heated to 180 °C in 30 min and held for 2 h. Then the temperature was increased to 550 °C in 4 h and held for another 6 h. After calcination, the white SBA-15 powder was obtained.

4.2. Synthesis of Two-Dimensional Ordered Mesoporous Cobalt–Manganese Oxide

A 0.8 M precursor solution was prepared by dissolving $Co(NO_3)_2 \bullet 6H_2O$ (ACS reagent, ≥98%; Sigma-Aldrich) and $Mn(NO_3)_2 \bullet 4H_2O$ (purum p.a., ≥97.0% (KT); Sigma-Aldrich) in the desired ratio in ethanol (absolute for analysis EMSURE ACS, ISO, Reag. Ph Eur; Merck). This precursor solution was impregnated into the SBA-15 by first mixing 70 vol% of the solution with the SBA-15 and stirring for one hour at room temperature in a 250 mL PP beaker. The suspension was then dried overnight at 40 °C. The dry powder was ground and mixed before calcination at 250 °C for 4 h at a heating rate of 5 °C/min. After calcination, the powder was ground and mixed again before impregnation with the remainder of the precursor solution as described above. Final calcination was performed in two steps, with the first step at 250 °C for 4 h at a heating rate of 5 °C/min and the second step at 500 °C for 6 h with a heating rate of 2 °C/min. After the final calcination, the SBA-15 template was removed using a 2 M NaOH solution at 70 °C.

4.3. Materials Characterization

The wide-angle powder XRD patterns were measured with a STOE theta/theta diffractometer in a Bragg–Brentano geometry equipped with a Cu K$\alpha_{1/2}$ X-ray source with a 0.03° 2θ acquisition step with 8 s per step at room temperature. The phase identification was based on the comparison of experimental data with the PDF-2 ICCD database.[41] Raman spectroscopy measurements were performed using a Renishaw inVia Raman Microscope and a 785 nm 330 mW laser, 1200 l/mm grading coupled with a 50x lens (Leica). Nitrogen physisorption measurements were performed using a 3Flex Micromeritics at 77 K and analyzed using the MicroActive data analysis software. Before the measurement, the samples were degassed at 120 °C at 1.33 mbar for 4 h. The BET surface area was typically calculated within 0.05–0.3 p/p°. The pore size distribution was calculated using the BJH method. TEM images, as well as high-resolution TEM images were recorded with Thermo Scientific Talso F200X microscope operated at 200 kV acceleration voltage. The images obtained were analyzed using the Gatan Microscopy Suite 3 software. SEM images were recorded with a Hitachi S5500 equipped with a field emission gun (FEG) operated at 30 kV acceleration voltage. The XAS measurements were performed at the SAMBA beamline of the SOLEIL synchrotron, operating with an electron beam current of 450 mA. The incident energy was selected by a Si (200) double crystal monochromator. Incident flux was ca. 1 × 1010 ph/s using a beam

size of 1 x 1 mm. The Mn and Co *K*-edge were utilized to conduct measurements in transmission mode. The samples were prepared by diluting the corresponding powder with cellulose in a pellet (Ø = 13 mm), followed by placement in the sample holder and sealing with Kapton tape. Calibration was performed using Mn and Co metal foils. The final spectra were normalized and processed using the Fastosh software.

4.4. Electrochemical Characterization

The OER measurements were carried out under alkaline conditions (1 M KOH) and the potential-current response was recorded with VSP-300 potentiostat (BioLogic) and the EC-Lab software. The measurements were conducted on a rotating disc electrode (Model: BluRev RDE, BioLogic) in a three-electrode setup. Both Pt wire and graphite rod (Ø 6 mm x 100 mm; Polymet – Reine Metalle) were used as the counter electrode. As a reference electrode, a RHE (HydroFlex; Gaskatel) was used. Working electrodes were prepared by drop casting 5.25 µL of catalyst ink onto 0.196 cm^2 glassy carbon (GC) electrodes, resulting in a mass loading of ~0.12 mg/cm^2. Before the drop casting, the GC electrodes were thoroughly cleaned by first polishing with MicroPolish Alumina suspension (1.0 µm and 0.05 µm particle size; Buehler) and then sonication in distilled water. The catalyst ink was prepared by dispersing 4.8 mg of catalyst powder in a mixture of 50 µL Nafion-117 (Sigma-Aldrich) and 1 mL solution of 75 vol% ultrapure water and 25 vol% isopropanol (anhydrous, 99.5 %; Sigma-Aldrich). The ink was sonicated until homogeneous. The electrolyte was degassed for at least 30 min with Ar, and the electrochemical cell was kept at 25 °C with a thermostat. LSV was performed within the potential range of 0.7–1.7 V versus RHE with a scan rate of 10 mV/s. CV was performed within the potential range of 0.7–1.6 V versus RHE at a scan rate of 50 mV/s. Electron impedance spectroscopy (EIS) was performed at 1.6 V versus RHE with a 5 mV amplitude within the 100 kHz to 100 mHz range. The RDE was rotated at 2000 RPM and the Ohmic drop was compensated at 85% for all measurements. The EIS was fitted to an equivalent circuit model using the Z-Fit feature in EC-Lab software.

4.5. In Situ Raman Spectroscopy

In situ Raman spectroscopy was performed using the same instrument as for traditional Raman spectroscopy using a customized electrochemical flow cell with a three-electrode system. A 785 nm 330 mW laser, 1200 l/mm grading coupled with a 50x lens (Leica) were used. The exposure time was 3 s with 20 accumulations and a laser power of 0.1%. The same Pt wire and reference electrode were used as described above. The working electrode was prepared by drop casting the same ink as described above on top of a roughened Au foil. The Au foil was electrochemically roughened by adapting the protocol as reported by Bell et al.[39] The used electrolyte was a 1 M KOH solution. The spectra were recorded during chronoamperometry measurements at a given potential step.

Supporting Information

The authors have cited additional references within the Supporting Information.[42]

Acknowledgments

This research was financially supported by the Deutsche Forschungsgemeinschaft (DFG, German Research Foundation), Projektnummer 388390466-TRR 247 (subproject C1) within the Collaborative Research Centre/Transregio 247 "Heterogeneous Oxidation Catalysis in the Liquid Phase" and by the Max Planck Society. H.T. thanks the Max Planck Society and the FUNCAT Centre, and the Spanish Ministry of Science, Innovation and Universities for the ATRAE grant. S. Palm and A. Kostis are acknowledged for EDX analysis and SEM images. A.K. acknowledges the Alexander von Humboldt Foundation for a Humboldt Research Fellowship. The authors thank Dr. G. Landrot and other beamline scientists for their assistance during the beam-time (proposal no.: 20240233) at SAMBA SOLEIL. The authors thank Jan Ternieden for the postmortem XRD analysis. The authors also thank Sebastian Leiting for the post-mortem XPS analysis.

Open access funding enabled and organized by Projekt DEAL.

Conflict of Interests

The authors declare no conflict of interest.

Data Availability Statement

The data that support the findings of this study are available from the corresponding author upon reasonable request.

Keywords: Cobalt manganese oxide · Electrocatalyst · Hard templating · In situ Raman · Oxygen evolution reaction

[1] Copernicus Climate Change Service (C3S) and World Meteorological Organization (WMO) **2025**.
[2] Climate Change 2022 - Mitigation of Climate Change: Working Group III Contribution to the Sixth Assessment Report of the Intergovernmental Panel on Climate Change, Cambridge University Press, Cambridge **2023**.
[3] M. Yu, E. Budiyanto, H. Tüysüz, *Angew. Chem., Int. Ed.* **2022**, *61*, e202103824.
[4] D. A. Corrigan, *J. Electrochem. Soc.* **1987**, *134*, 377–384.
[5] A. N. Løvik, C. Hagelüken, P. Wäger, *Sustain. Mater. Technol.* **2018**, *15*, 9–18.
[6] X. Li, Y. Sun, Q. Wu, H. Liu, W. Gu, X. Wang, Z. Cheng, Z. Fu, Y. Lu, *J. Am. Chem. Soc.* **2019**, *141*, 3121–3128.
[7] H. Jin, J. Wang, D. Su, Z. Wei, Z. Pang, Y. Wang, *J. Am. Chem. Soc.* **2015**, *137*, 2688–2694.
[8] J. L. Gautier, C. Cabezas, *J. Electroanal. Chem. Interfacial Electrochem.* **1983**, *159*, 137–153.
[9] A. Li, S. Kong, C. Guo, H. Ooka, K. Adachi, D. Hashizume, Q. Jiang, H. Han, J. Xiao, R. Nakamura, *Nat. Catal.* **2022**, *5*, 109–118.
[10] J. Villalobos, D. M. Morales, D. Antipin, G. Schuck, R. Golnak, J. Xiao, M. Risch, *ChemElectroChem* **2022**, *9*, e202200482.
[11] C. Li, X. Han, F. Cheng, Y. Hu, C. Chen, J. Chen, *Nat. Commun.* **2015**, *6*, 7345.
[12] A. L. Silva, L. M. Esteves, L. P. C. Silva, V. S. Ramos, F. B. Passos, N. M. F. Carvalho, *RSC Adv.* **2022**, *12*, 26846–26858.
[13] E. Rios, J. L. Gautier, G. Poillerat, P. Chartier, *Electrochim. Acta* **1998**, *44*, 1491–1497.

[14] K. Lankauf, K. Cysewska, J. Karczewski, A. Mielewczyk-Gryń, K. Górnicka, G. Cempura, M. Chen, P. Jasiński, S. Molin, *Int. J. Hydrogen Energy* **2020**, *45*, 14867–14879.
[15] B. He, P. Hosseini, D. Escalera-López, J. Schulwitz, O. Rüdiger, U. Hagemann, M. Heidelmann, S. DeBeer, M. Muhler, S. Cherevko, K. Tschulik, T. Li, *Adv. Energy Mater.* **2025**, *15*, 2403096.
[16] A.-H. Lu, F. Schüth, *Adv. Mater.* **2006**, *18*, 1793–1805.
[17] X. Deng, K. Chen, H. Tüysüz, *Chem. Mater.* **2017**, *29*, 40–52.
[18] V. G. Hadjiev, M. N. Iliev, I. V. Vergilov, *J. Phys. C: Solid State Phys.* **1988**, *21*, L199–L201.
[19] C. F. Windisch, Jr., G. J. Exarhos, S. K. Sharma, *J. Appl. Phys.* **2002**, *92*, 5572–5574.
[20] M. Thommes, K. Kaneko, A. V. Neimark, J. P. Olivier, F. Rodriguez-Reinoso, J. Rouquerol, K. S. W. Sing, *Pure. Appl. Chem.* **2015**, *87*, 1051–1069.
[21] O. Knop, K. I. G. Reid, Sutarno, Y. N., *Can. J. Chem.* **1968**, *46*, 3463–3476.
[22] D. Jarosch, *Mineral. Petrol.* **1987**, *37*, 15–23.
[23] V. Kunzl, *Collect. Czech. Chem. Commun.* **1932**, *4*, 213–224.
[24] O. A. Bulavchenko, T. N. Afonasenko, A. V. Ivanchikova, V. Y. Murzin, A. M. Kremneva, A. A. Saraev, V. V. Kaichev, S. V. Tsybulya, *Inorg. Chem.* **2021**, *60*, 16518–16528.
[25] C. C. L. McCrory, S. Jung, I. M. Ferrer, S. M. Chatman, J. C. Peters, T. F. Jaramillo, *J. Am. Chem. Soc.* **2015**, *137*, 4347–4357.
[26] I. Zaharieva, D. González-Flores, B. Asfari, C. Pasquini, M. R. Mohammadi, K. Klingan, I. Zizak, S. Loos, P. Chernev, H. Dau, *Energ. Environ. Sci.* **2016**, *9*, 2433–2443.
[27] J. Villalobos, R. Golnak, L. Xi, G. Schuck, M. Risch, *J. Phys.: Energy* **2020**, *2*, 034009.
[28] Q. Gao, C. Ranjan, Z. Pavlovic, R. Blume, R. Schlögl, *ACS Catal.* **2015**, *5*, 7265–7275.
[29] A. Bergmann, E. Martinez-Moreno, D. Teschner, P. Chernev, M. Gliech, J. F. de Araújo, T. Reier, H. Dau, P. Strasser, *Nat. Commun.* **2015**, *6*, 8625.
[30] E. Budiyanto, S. Zerebecki, C. Weidenthaler, T. Kox, S. Kenmoe, E. Spohr, S. DeBeer, O. Rüdiger, S. Reichenberger, S. Barcikowski, H. Tüysüz, *ACS Appl. Mater. Interfaces* **2021**, *13*, 51962–51973.
[31] M. Yu, F. Waag, C. K. Chan, C. Weidenthaler, S. Barcikowski, H. Tüysüz, *ChemSusChem* **2020**, *13*, 520–528.
[32] J. B. Gerken, J. G. McAlpin, J. Y. C. Chen, M. L. Rigsby, W. H. Casey, R. D. Britt, S. S. Stahl, *J. Am. Chem. Soc.* **2011**, *133*, 14431–14442.
[33] A. K. Tomar, U. N. Pan, N. H. Kim, J. H. Lee, *ACS Energy Lett.* **2023**, *8*, 565–573.
[34] A. Kumar, M. Gil-Sepulcre, J. P. Fandré, O. Rüdiger, M. G. Kim, S. DeBeer, H. Tüysüz, *J. Am. Chem. Soc.* **2024**, *146*, 32953–32964.
[35] Z.-F. Huang, J. Song, Y. Du, S. Xi, S. Dou, J. M. V. Nsanzimana, C. Wang, Z. J. Xu, X. Wang, *Nat. Energy* **2019**, *4*, 329–338.
[36] M. E. G. Lyons, M. P. Brandon, *J. Electroanal. Chem.* **2009**, *631*, 62–70.
[37] R. L. Doyle, M. E. G. Lyons, *J. Electrochem. Soc.* **2013**, *160*, H142–H154.
[38] E. Budiyanto, M. Yu, M. Chen, S. DeBeer, O. Rüdiger, H. Tüysüz, *ACS Appl. Energy Mater.* **2020**, *3*, 8583–8594.
[39] B. S. Yeo, A. T. Bell, *J. Am. Chem. Soc.* **2011**, *133*, 5587–5593.
[40] A. Moysiadou, S. Lee, C.-S. Hsu, H. M. Chen, X. Hu, *J. Am. Chem. Soc.* **2020**, *142*, 11901–11914.
[41] S. Gates-Rector, T. Blanton, *Powder Diffr.* **2019**, *34*, 352–360.
[42] M. C. Biesinger, B. P. Payne, A. P. Grosvenor, L. W. M. Lau, A. R. Gerson, R. S. C. Smart, *Appl. Surf. Sci.* **2011**, *257*, 2717–2730.

Manuscript received: July 24, 2025
Revised manuscript received: August 20, 2025
Accepted manuscript online: September 10, 2025
Version of record online: ■■, ■■